Forschungszentrum Karlsruhe
in der Helmholtz-Gemeinschaft

Wissenschaftliche Berichte
FZKA7094

A Fracture Mechanics Analysis of the DCDC Specimen

T. Fett, G. Rizzi

Institut für Materialforschung

April 2005

FORSCHUNGSZENTRUM KARLSRUHE

in der Helmholtz-Gemeinschaft

Wissenschaftliche Berichte

FZKA 7094

A FRACTURE MECHANICS ANALYSIS OF THE DCDC SPECIMEN

T. Fett, G. Rizzi

Institut für Materialforschung

Forschungszentrum Karlsruhe GmbH, Karlsruhe

2005

Impressum der Print-Ausgabe:

Als Manuskript gedruckt

Forschungszentrum Karlsruhe GmbH
Postfach 3640, 76021 Karlsruhe

Mitglied der Hermann von Helmholtz-Gemeinschaft
Deutscher Forschungszentren (HGF)

ISSN 0947-8620

urn:nbn:de:0005-070948

A fracture mechanics analysis of the DCDC specimen

Abstract:

The “double cleavage drilled compression” (DCDC) specimen is a rectangular bar with a circular hole in its centre that is loaded by compressive stresses. Due to the hole, positive stresses are generated in the vicinity that cause positive mode-I stress intensity factors. This specimen is used for the determination of crack growth under mode-I and in a modified version under mixed-mode loading conditions. A fracture mechanics analysis is presented on the basis of finite element computations. After compilation of literature results on mixed-mode stress intensity factors and T-stresses, weight functions for mode I and mode II are derived. The consequences of load misalignment and crack kinking are shown. Since stress intensity factor results from literature are available for long cracks compared with the hole radius only, also short-crack solutions are derived by use of the weight function technique. These results allow to discuss the generation of the initial cracks necessary for fracture mechanics tests.

In several papers, the side surface displacements were reported and discussed with respect to the occurrence of plasticity effects in glass. In order to decide whether deviations from the pure linear-elastic material behaviour are measured, it is necessary to know the elastic response. Therefore, a 3-dimensional finite element study is performed. It exhibits depression and uplifting of the free surface very similar to the results found in literature.

Eine bruchmechanische Analyse der DCDC-Probe

Kurzfassung:

Die DCDC-Probe besteht aus einem rechteckigen Stab mit mittig gebohrtem zylindrischen Loch, der in Stablängsachsenrichtung mit Druck belastet wird. Aufgrund des Loches werden in dessen Umgebung Zugspannungen erzeugt, die bei Anwesenheit von Rissen zu positiven Spannungsintensitätsfaktoren K_I führen. Die DCDC-Probe wird für bruchmechanische Versuche unter reiner Mode-I-Beanspruchung und in einer modifizierten Version mit exzentrischer Lochanordnung für Mixed-Mode-Versuche verwendet.

Nach einer Zusammenstellung von Literaturlösungen für die Spannungsintensitätsfaktoren K_I und K_{II} sowie die T-Spannung werden die beiden Gewichtsfunktionen h_I und h_{II} ermittelt. Es werden dann der Einfluss einer Exzentrizität der Lastaufbringung und die Auswirkung einer Rissabknickung betrachtet.

Während in der Literatur nur die bruchmechanischen Belastungsgrößen für relativ lange Risse (ein Vielfaches des Lochradius) verfügbar sind, werden zur Beschreibung der Rissinitiierungsphase auch Lösungen für kleine Risse benötigt. Diese werden mittels der Gewichtsfunktion bestimmt.

In neueren Publikationen werden mit dem Atomkraftmikroskop aufgenommene Höhenprofile auf den Seitenflächen dazu verwendet, einen Plastizitätseffekt bei Glas zu diskutieren. Hierzu ist aber unabdingbar, die durch rein linear-elastisches Materialverhalten nahe der Rissspitze erzeugten Höhen-Profile zu bestimmen. Es wurden hierzu 3-D-Rechnungen mittels finiter Elemente durchgeführt. Diese führten zu Höhenprofilen, die gleiche Charakteristiken wie die Experimente aufweisen.

Contents

1. Introduction 1

2. Literature results 1

2.1 Symmetric specimen with centric hole 1

2.2 Asymmetric specimen with hole offset 3

3. Weight function 6

3.1 Small-crack solution 6

3.2 Long-crack solutions 7

3.3 Finite element computations 8

4. Eccentricity of loading 11

5. Stress intensity factor of kinked cracks 12

6. Short-crack behaviour 16

6.1 Limit case $R/H \to 0$ 16

6.2 Influence of finite specimen height 18

7. Spontaneous crack propagation 20

8. 3-dimensional analysis 22

8.1 Straight crack 22

8.1.1 Stress intensity factor and T-stress 22

8.1.2 Surface displacements 23

8.2 Influence of a curved crack front 25

9. A modification of the path stability relation for DCDC specimens 28

References 30

1. Introduction

The “double cleavage drilled compression” (DCDC) specimen is a rectangular bar with a circular hole in its centre that is loaded by compressive stresses. The test specimen shown in Fig. 1.1 is used for the determination of crack growth under mode-I [1,2,3,4]. Using a modified version, crack growth is determined under mixed-mode loading conditions [1,2]. Whereas solutions for stress intensity factors and T-stress are available in literature, there is a lack in weight functions. After a compilation of literature results on mixed-mode stress intensity factors and T-stresses, weight functions for mode I and mode II will be derived in this report. The consequences of load misalignment and crack kinking will be outlined.

In several papers on DCDC tests with glass specimens, the side surface displacements were reported and discussed with respect to the occurrence of plasticity effects in glass. In order to decide whether deviations from the pure linear-elastic material behaviour are measured, it is necessary to know the elastic response. Therefore, a 3-dimensional finite element study was performed. It exhibits depression and uplifting of the free surface very similar to the results found in literature.

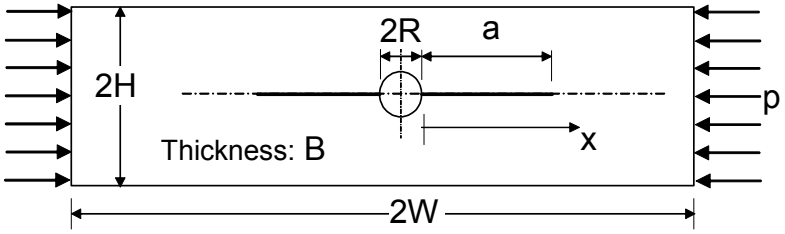

Fig. 1.1 Standard DCDC specimen.

2. Literature results

A fracture mechanics analysis of crack propagation requires knowledge of the stress intensity factors and the T-stress.

Especially for the assessment of crack path stability, it is of importance to know the T-stress term, i.e. the first regular stress term in the Williams series expansion. Using the singular stress term and the first regular term, the near-tip stress field of a cracked body can be described appropriately by

$$\sigma_{ij} = \frac{K_I}{\sqrt{2\pi r}} f_{ij}(\varphi) + \sigma_{ij,0} \quad , \quad \sigma_{ij,0} = \begin{pmatrix} \sigma_{xx,0} & \sigma_{xy,0} \\ \sigma_{yx,0} & \sigma_{yy,0} \end{pmatrix} = \begin{pmatrix} T & 0 \\ 0 & 0 \end{pmatrix} \tag{2.1}$$

where f_{ij} are the well-known angular functions for the singular stress contribution.

2.1 Symmetric specimen with a central hole

Stress intensity factor solutions for the DCDC specimen are available in literature. The stress intensity factor of the symmetric test specimen, b/R=0, was determined by He et al. [1], who proposed

$$\frac{|p|\sqrt{\pi R}}{K_I} = \frac{1}{F} = \frac{H}{R} + \left[0.235\frac{H}{R} - 0.259\right]\frac{a}{R} \tag{2.2}$$

(see also [5]). This relation is shown by the dashed curves in Fig. 2.1a.

Based on the finite element results of Fig. 2.1a (circles), the geometric function for the stress intensity factors was fitted as (see [6])

$$\frac{1}{F} = -0.37 + 1.116\frac{H}{R} + \left[0.216\frac{H}{R} - 0.1575\right]\frac{a}{R} \tag{2.3}$$

This relation is plotted in Fig. 2.1a as the solid curves.

The T-stress results as [6]

$$\frac{1}{(T/|p|)+1} = -1.39 + 1.18\frac{H}{R} + \left[0.2\frac{H}{R} - 0.24\right]\frac{a}{R} \tag{2.4}$$

as shown in Fig. 2.1b.

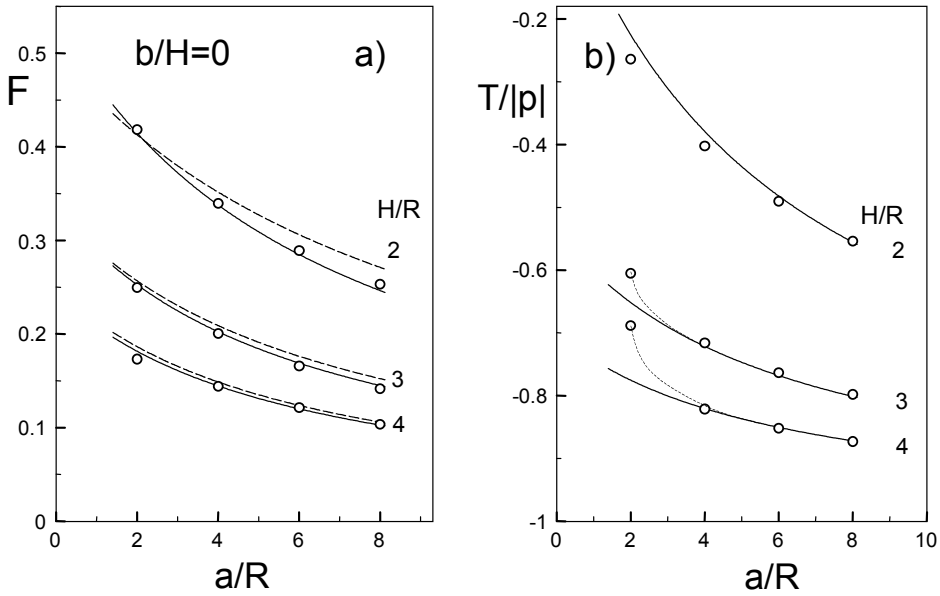

Fig. 2.1 a) Geometric function for the stress intensity factor (symbols: finite element results, solid curves: fit relation eq.(2.3), dashed curves: eq.(2.2) from [1], b) T-stress (symbols: finite element results, solid curves: fit relation eq.(2.4).

The biaxiality ratio β according to Leevers and Radon [7]

$$\beta = \frac{T\sqrt{\pi a}}{K_I} \tag{2.5}$$

is plotted in Fig. 2.2a. The symbols represent the finite element results. The dashed curves were computed from eq.(2.2) and eq.(2.4), the solid curves from eq.(2.3) and eq.(2.4). For the mostly chosen geometry H/R=4 (see e.g. [3,4]), the biaxiality ratio may be expressed by a simple straight-line approximation

$$\beta = 1.2 - 3.11\,a/R \tag{2.6}$$

as introduced in Fig. 2.2b.

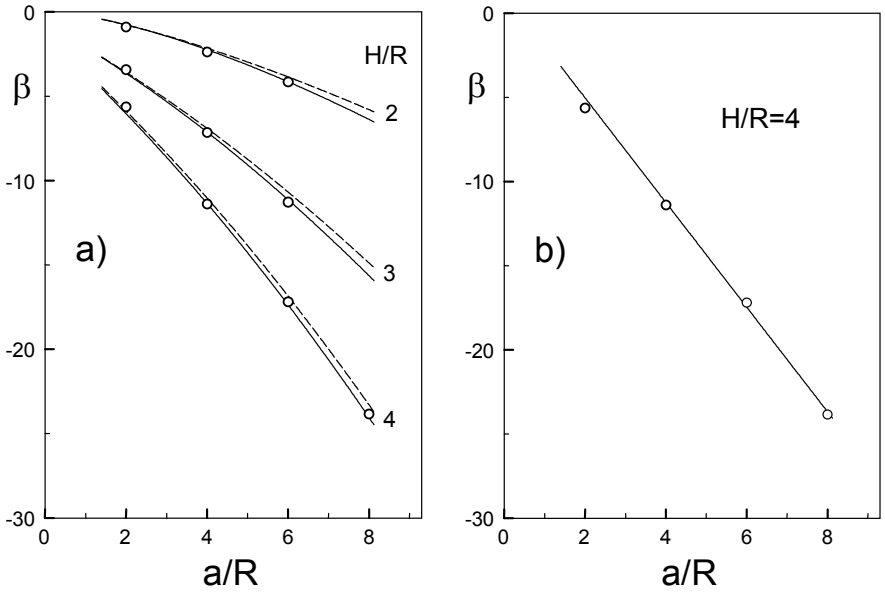

Fig. 2.2 Biaxiality ratio obtained from the results of Figs. 2.1a and 2.1b; a) symbols: finite element results [6], solid curves: based on data fit relation eq.(2.3), dashed curves: eq.(2.2), from [1], b) simplified straight-line fit according to eq.(2.6).

2.2 Asymmetric specimen with hole offset

For mixed-mode crack loading, the asymmetric DCDC specimen was applied [2]. This specimen with an offset of the hole is shown in Fig. 2.3 (see [5]).

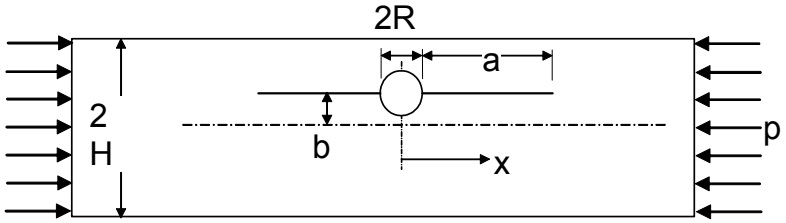

Fig. 2.3 DCDC specimen with hole offset for mixed-mode tests.

The mode-I stress intensity factors shown in Fig. 2.4a were fitted for $a/R \geq 4$ [6] according to

$$\frac{1}{F_I} = c_0 + c_1 \frac{H}{R} + \left[c_2 \frac{H}{R} + c_3 \right] \frac{a}{R} \tag{2.7a}$$

with the coefficients

$$c_0 = -0.3703 - 0.2706\,(b/R) - 0.2716\,(b/R)^2 \tag{2.7b}$$

$$c_1 = 1.1163 + 0.1864\,(b/R) - 0.0140\,(b/R)^2 \tag{2.7c}$$

$$c_2 = 0.2160 - 0.0326\,(b/R) + 0.0040\,(b/R)^2 \tag{2.7d}$$

$$c_3 = -0.1575 + 0.0176\,(b/R) + 0.0040\,(b/R)^2 \tag{2.7e}$$

For the mostly used geometry H/R=4 and small misalignments b<<R, it holds

$$1/F_1 = 4.1 + 0.475b/R + [0.706 - 0.113b/R]a/R \tag{2.8}$$

Mode-II stress intensity factors are given in Fig. 2.4b and 2.4c in the form of the mixed-mode ratio K_{II}/K_I.

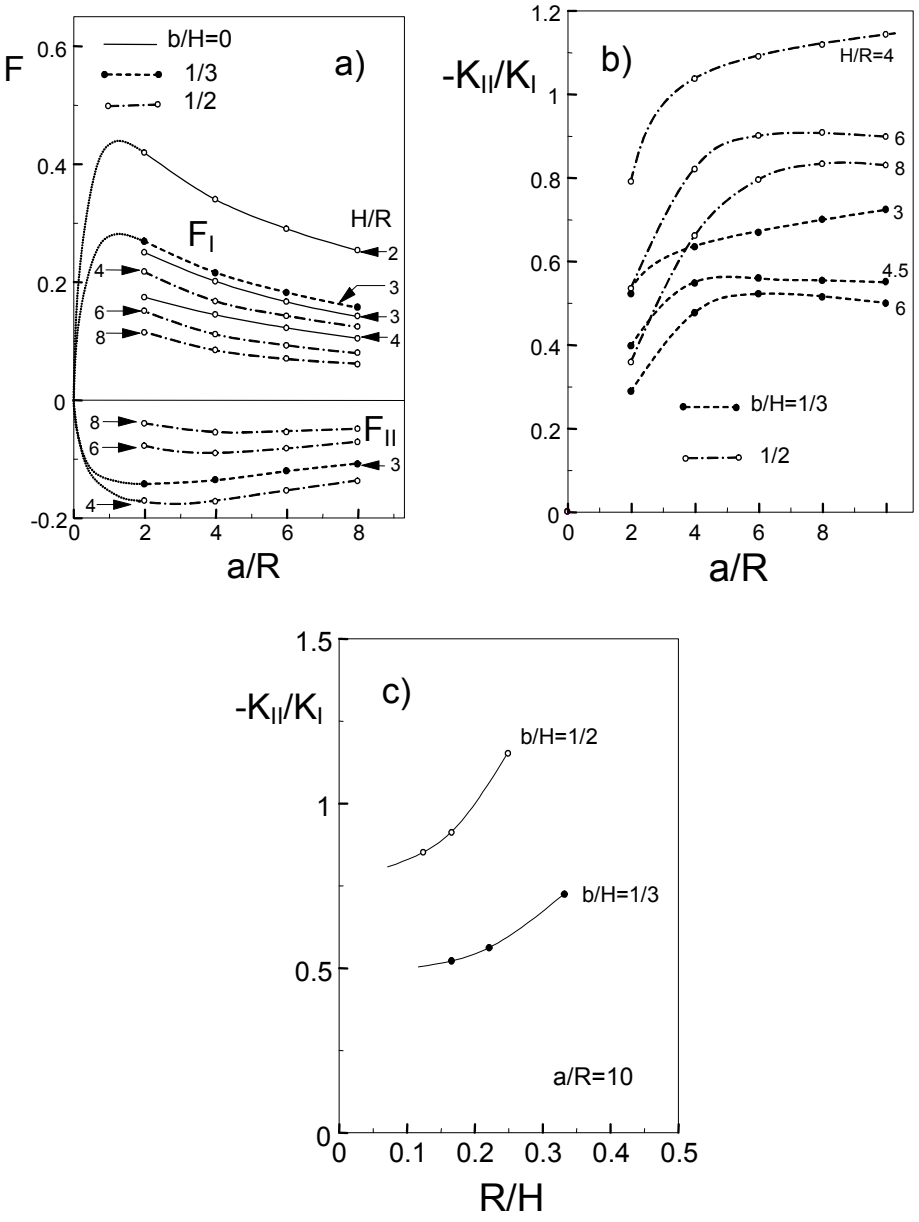

Fig. 2.4 a) Mixed-mode stress intensity factors, b) mode mixity, c) mode mixity at a/R=10 [6].

Figure 2.5a represents the T-stress results, and in Fig. 2.5b the biaxiality ratio β, eq.(2.5), is plotted according to [7]. Since β is strongly negative, growing cracks must exhibit a very high path stability [8,9,10].

The data of Fig. 2.5a were fitted for $a/R \geq 4$ by the equation of

$$\frac{1}{(T/|p|)+1} = f_0 + f_1\frac{H}{R} + \left[f_2\frac{H}{R} + f_3\right]\frac{a}{R} \tag{2.9a}$$

with the coefficients [6]

$$f_0 = -1.3903 + 0.9310(b/R) - 0.1038(b/R)^2 \tag{2.9b}$$

$$f_1 = 1.1801 - 0.3575(b/R) + 0.0222(b/R)^2 \tag{2.9c}$$

$$f_2 = 0.2003 + 0.1061(b/R) - 0.0039(b/R)^2 \tag{2.9d}$$

$$f_3 = -0.2397 - 0.3471\ (b/R) - 0.0827\ (b/R)^2 \tag{2.9e}$$

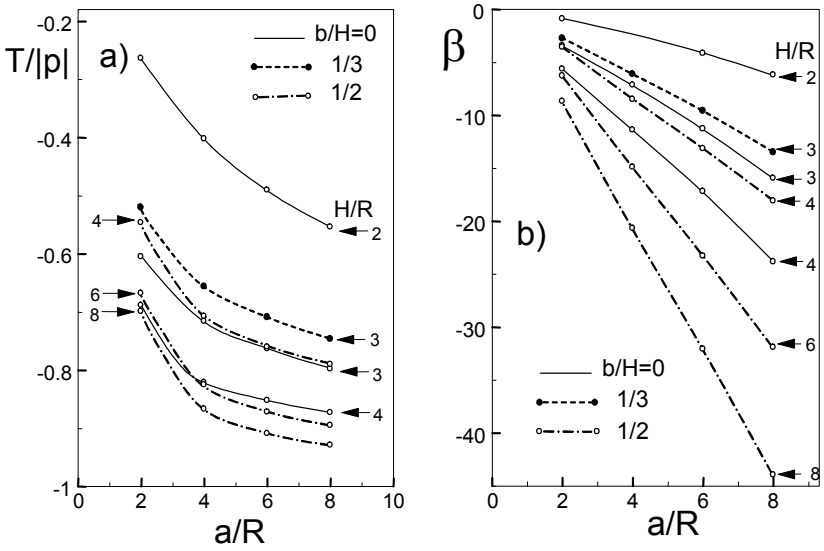

Fig. 2.5 a) T-stress of a DCDC specimen, b) biaxiality ratio β.

3. Weight functions

3.1 Small-crack solution

Weight functions are an important tool for the computation of stress intensity factors for the case of known stresses in the uncracked component. If σ_y is the normal stress on the prospective crack line and τ_{xy} is the shear stress in this plane, the stress intensity factors result from

$$K_I = \int_0^a h_I \sigma_y(x) dx \tag{3.1}$$

$$K_{II} = \int_0^a h_{II} \tau_{xy}(x) dx \tag{3.2}$$

where a is the crack length and x the coordinate along the crack. In many cases, the mode-I weight function is available from literature.

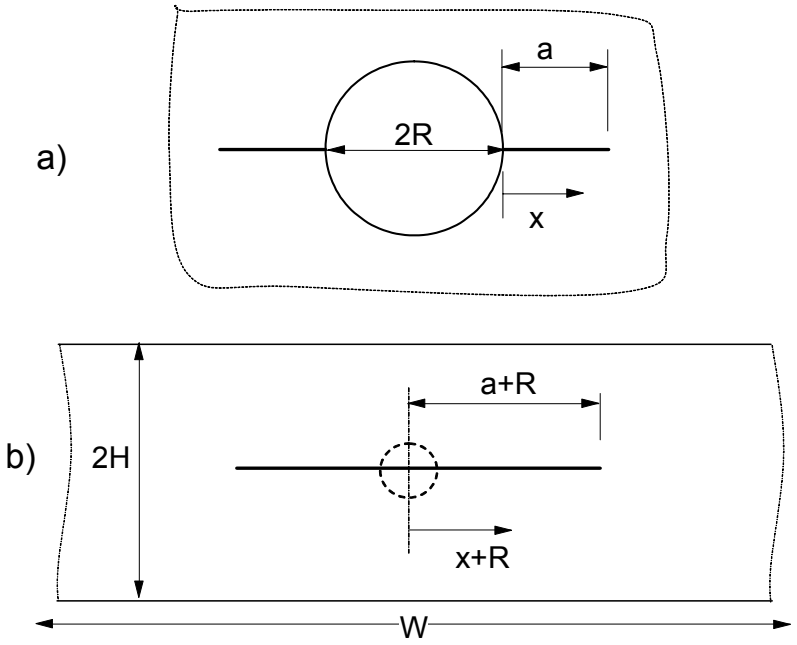

Fig. 3.1 Two limit cases for the DCDC specimen: a) a pair of cracks emanating from a circular hole in an infinite body, b) crack parallel to the edges of a strip of finite height.

Two limit cases for the weight function can be identified. The weight function for cracks emanating from a circular hole in an infinite body (see Fig. 3.1a) can be written as

$$h_{hole} = \sqrt{\frac{2}{\pi a}}\left(\frac{1}{\sqrt{1-x/a}} + D_1\sqrt{1-x/a} + D_2(1-x/a)^{3/2}\right) \tag{3.3}$$

with the coefficients D_1 and D_2 reported in [11] in a tabulated form. These coefficients represented by the circles in Fig. 3.2 may be expressed by

$$D_1 = 0.155 + 0.435\exp(-6.86a/R) \tag{3.4}$$

$$D_2 = 0.101 + 0.144\exp(-2.911(a/R)^{3/2}) \tag{3.5}$$

These approximations are plotted as the curves in Fig. 3.2.

3.2 Long-crack solutions

The weight function for a crack in a plate strip (Fig. 3.1b) is given in Chapter 6.9 of [11]. With the origin of the crack at the circle, it holds

$$h_{strip} = \frac{2}{\sqrt{\pi(a+R)}}\left(\frac{1}{\sqrt{1-\rho^2}} + B\sqrt{1-\rho^2}\right), \quad \rho = \frac{x+R}{a+R} \tag{3.6}$$

with

$$B = 2(1+\alpha)^{3/2}[0.6515 + 0.3485\exp(-4.304\alpha)] - 2\,, \quad \alpha = (a+R)/H \tag{3.7}$$

as plotted in Fig. 3.3. For $a/R \geq 1$ and H/R, an approximate weight function for the DCDC specimen reads

$$h_{DCDC} \approx \sqrt{\frac{2}{\pi a}}\left(\frac{1}{\sqrt{1-x/a}} + C\sqrt{1-x/a}\right) \tag{3.8}$$

with the coefficient C shown in Fig. 3.3. For $2 \leq a/R \leq 8$ this dependency may be expressed by

$$C \cong -0.425 + 0.9944(a/R) + 0.021(a/R)^2 \tag{3.9}$$

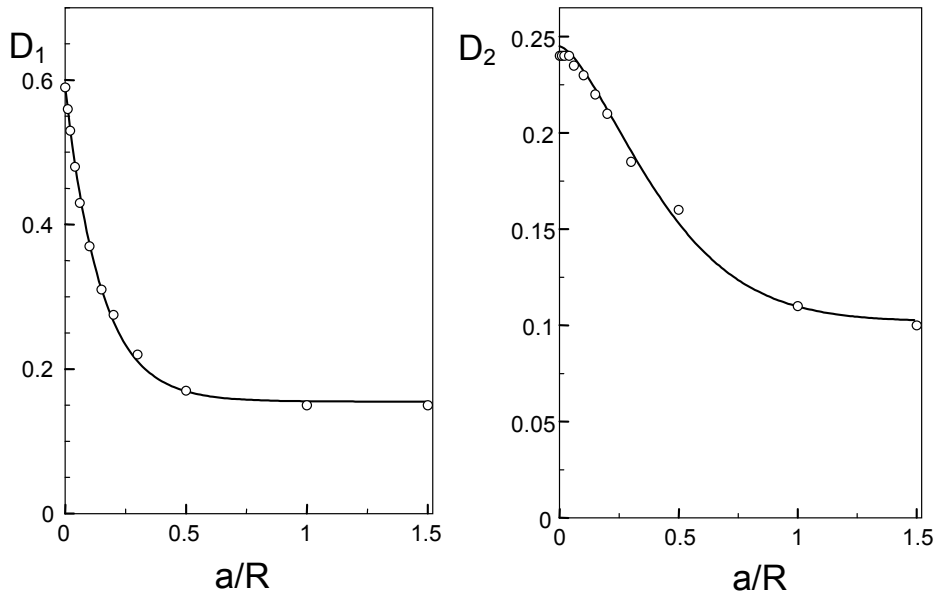

Fig. 3.2 Coefficients for the weight function of a pair of cracks emanating from a circular hole in an infinite body (circles: data from [11], curves: approximate representation according to eqs.(3.4) and (3.5).

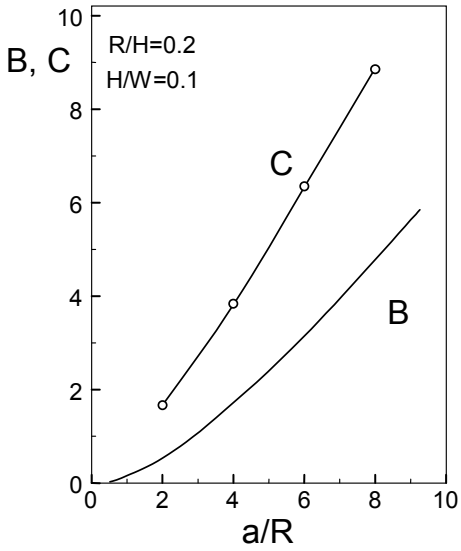

Fig. 3.3 Coefficients for eqs.(3.6) and (3.8).

3.3 Finite element computations

In order to determine the T-stress term, finite element computations were performed. For the 2-dimensional computations of straight cracks, a finite element net of about 970 elements with 3100 nodes was used. For the kinked cracks, the numbers were 900 elements with 2800 nodes and in the case of the 3-dimensional analysis, we used 5600 elements with 27000 nodes. The crack tip region was modelled by collapsed two-dimensional elements. The computations were carried out with ABAQUS Version 6.2 which provides individual stress intensity factors K_{I} and K_{II} as well as the T-stress. For this purpose, ABAQUS employs an interaction integral according to Shih and Aroso [12]. The accuracy of the results is expected to be better than 2%.

Figure 3.4 shows stress intensity factors for pairs of concentrated normal forces P and shear forces Q acting symmetrically on the faces of the crack at distance x. These stress intensity factors are identical with the weight functions. It becomes obvious that for shear loading the total weight function differs only slightly from the limit cases represented by the singular term (dashed curves).

The stress intensity factors of Fig. 3.4 were fitted by the relation

$$h_{I,II} = \sqrt{\frac{2}{\pi a}}\left(\frac{1}{\sqrt{1-x/a}} + D_1^{(I,II)}\sqrt{1-x/a} + D_2^{(I,II)}(1-x/a)^{3/2} \right) \qquad (3.10)$$

with the coefficients for a/R=4: D_1=3.379, D_2=0.591 for mode-I and D_1=0.5687, D_2=-0.3493 for mode-II. The dependency of eq. (3.10) with these parameters is entered in Fig. 3.4 as the solid curves.

The coefficients for several crack lengths are compiled in Table 3.1. Values of intermediate lengths can be obtained by parabolic interpolation. Table 3.2 presents the coefficients for the case of "one-side loading" as illustrated in Fig. 3.5.

Stress intensity factors for antisymmetrically applied shear forces (Fig. 3.6) are given in Table 3.3.

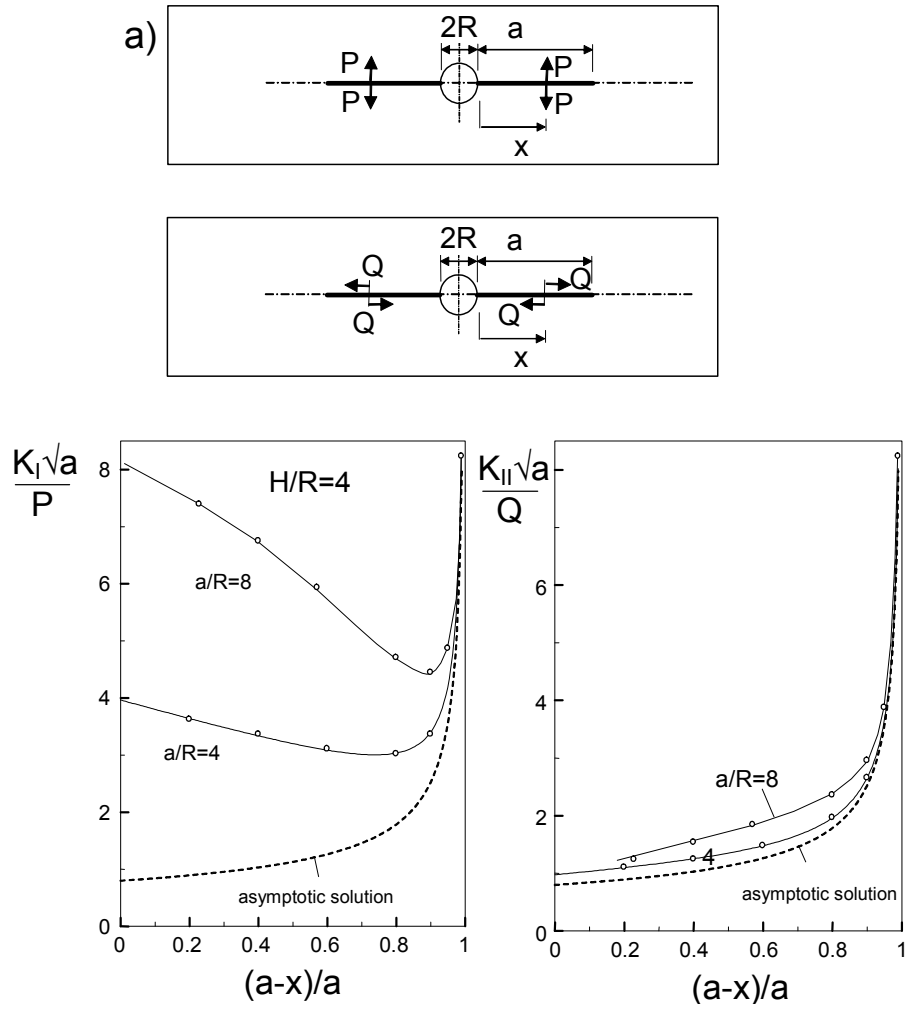

Fig. 3.4 a) Symmetric loading by point forces acting on the crack, b) stress intensity factors for pairs of normal stresses, c) stress intensity factor for shear forces.

Crack length a/R	Mode	$D_1^{(I)}$	$D_2^{(I)}$
2	I	1.465	0.208
4	I	3.379	0.591
6	I	5.561	1.184
8	I	8.222	1.482
Crack length a/R	Mode	$D_1^{(II)}$	$D_2^{(II)}$
2	II	0.1460	0.1843
4	II	0.5687	-0.3493
6	II	1.266	-1.132
8	II	2.034	-2.020

Table 3.1 Coefficients for the weight function representation (3.10) under symmetric loading.

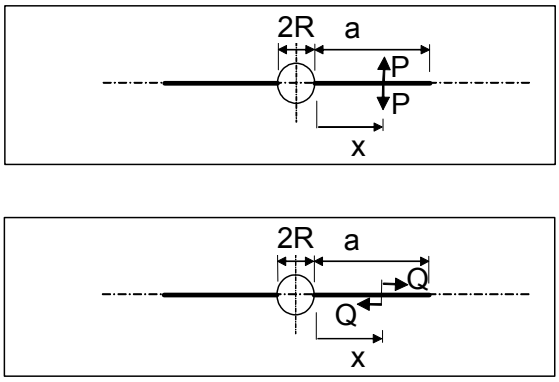

Fig. 3.5 One-side loading by point forces acting on the crack.

Crack length a/R	Mode	$D_1^{(I)}$	$D_2^{(I)}$
2	I	0.6988	-0.0445
4	I	2.242	-0.379
6	I	4.226	-0.8553
8	I	6.740	-1.816
Crack length a/R	Mode	$D_1^{(II)}$	$D_2^{(II)}$
2	II	0.4529	0.1358
4	II	1.0752	-0.1948
6	II	1.8564	-0.7194
8	II	2.704	-1.413

Table 3.2 Coefficients for the weight function representation (3.10) under one-side loading.

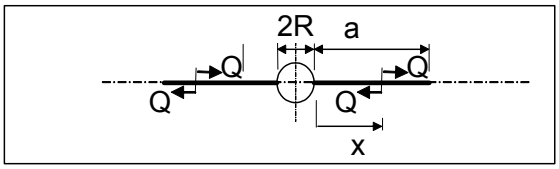

Fig. 3.6 Antisymmetric shear loading.

Crack length a/R	Mode	$D_1^{(II)}$	$D_2^{(II)}$
2	II	0.7594	0.0879
4	II	1.600	-0.0674
6	II	2.449	-0.3095
8	II	3.373	-0.8041

Table 3.3 Coefficients for the weight function representation (3.10) under anti-symmetric shear loading.

4. Eccentricity of loading

A possibility of misalignment is an offset y_P between the externally applied force P and the symmetry axis of the specimen (see Fig. 4.1). This eccentricity gives rise to a moment

$$M_b = P \times y_P \tag{4.1}$$

and bending stresses in the specimen. Whereas for small y_P/H the mode-I stress intensity factor is hardly affected, a mode-II stress intensity factor contribution is created, as shown in Fig. 4.2 for H/R=4 in normalised form. This effect does not only occur for point forces. Also in the case of a non-symetrically distributed load, a moment results as

$$M_b = \int_{-H}^{H} p(y) y dy \tag{4.2}$$

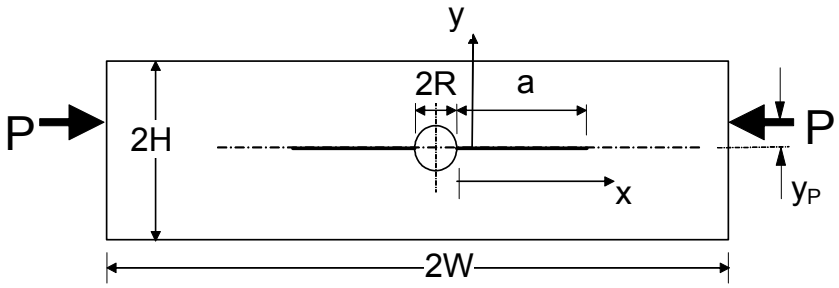

Fig. 4.1 DCDC specimen under eccentric loading.

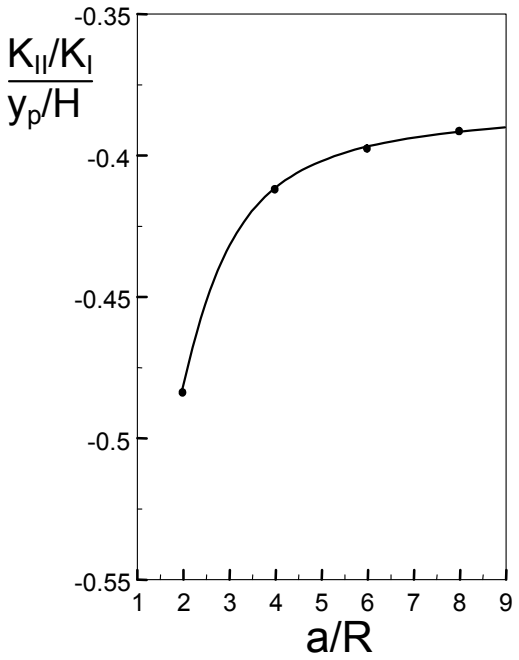

Fig. 4.2 Mode-II stress intensity factor caused by a misalignment y_P of the externally applied load P.

5. Stress intensity factors of kinked cracks

The stress intensity factors of kinked cracks (Fig. 5.1) were determined for H/R=4 and a/R=4 by finite element computations. The results are shown in Fig. 5.2 as a function of the kink length ℓ and the kink angle φ.

Under pure mode-I loading, the stress intensity factors for the kink, K_{I}, and K_{II}, can be expressed roughly by the stress intensity factor for the original (unkinked) crack, k_{I}, using the simple expressions of

$$K_I = k_I\, g_{11} + T\, b_1 \sqrt{\ell} \tag{5.1}$$

$$K_{II} = k_I\, g_{21} + T\, b_2 \sqrt{\ell} \tag{5.2}$$

with the angular functions

$$g_{11} = \cos^3(\beta/2) \tag{5.3}$$

$$g_{21} = \sin(\beta/2)\cos^2(\beta/2) \tag{5.4}$$

and the coefficients b_1 and b_2 given in [8,13]

$$b_1 = \sqrt{\frac{8}{\pi}}\sin^2\beta \tag{5.5}$$

$$b_2 = -\sqrt{\frac{8}{\pi}}\sin\beta\cos\beta \tag{5.6}$$

The results of Fig. 5.2 were plotted again as functions of g_{11} and g_{21}. Roughly, a straight-line behaviour is found. The deviations from a straight line indicate the influence of the T-stress term in eqs.(5.1) and (5.2).

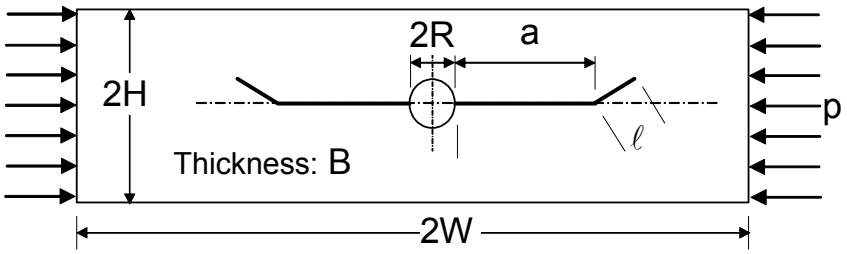

Fig. 5.1 DCDC specimen with symmetrically kinked cracks.

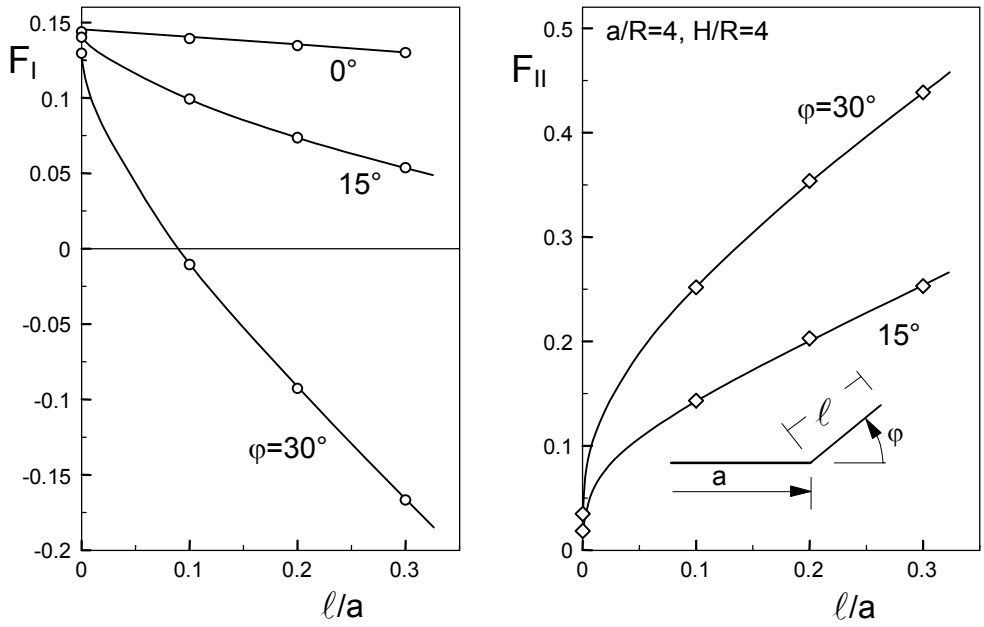

Fig. 5.2 Mixed-mode stress intensity factors for a kinked crack (Fig. 5.1). Geometry: a/R=4, H/R=4.

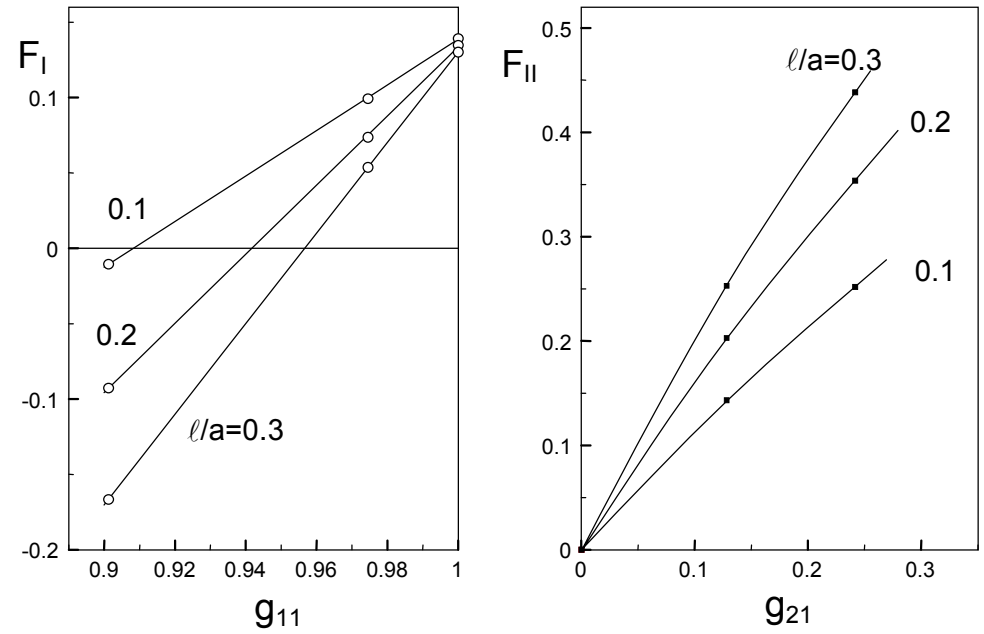

Fig. 5.3 Mixed-mode stress intensity factors for a kinked crack (Fig. 5.1) plotted vs. the angular functions g_{11} and g_{21}.

A kink at only one side is illustrated in Fig. 5.4. Figures 5.5a and 5.5b show the mixed-mode stress intensity factors for a kink angle of φ=5° and the geometric parameters a/R=4 and H/R=4. The kink is located at point (A) and the stress intensity factors are evaluated for the crack tip at location (B). The mode-I stress intensity factor at (B) is hardly affected by the kink. The mode-II stress intensity factor is roughly proportional to the kink length ℓ.

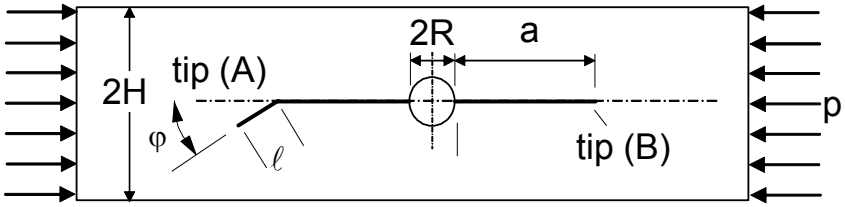

Fig. 5.4 DCDC specimen with a kink at point (A).

Figures 5.5c and 5.5d show the influence of the kink angle φ. The mode-II stress intensity factor K_{II} at point (B) is proportional to the kink angle. Consequently, it holds

$$K_{II,(B)} \propto (\ell / a)^2 \varphi \tag{5.7}$$

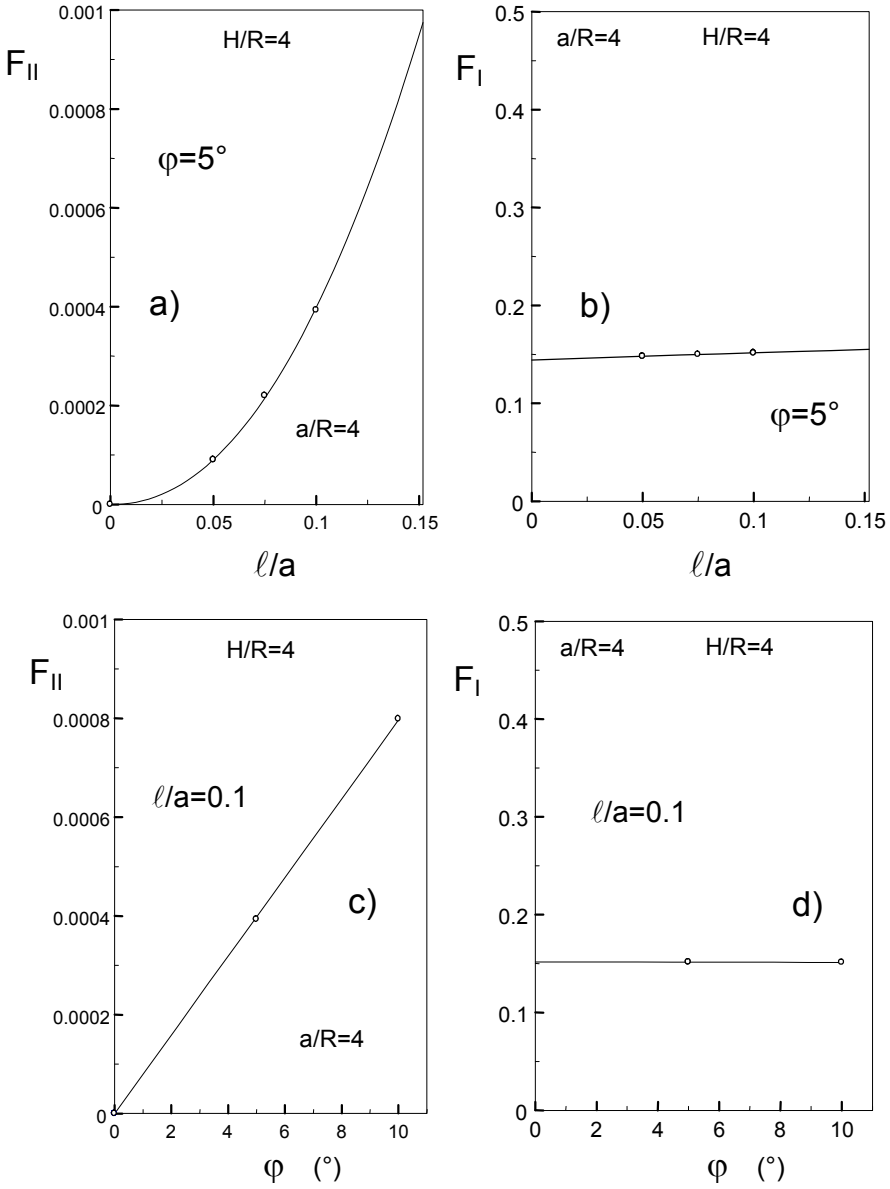

Fig. 5.5 Mixed-mode stress intensity factors at point (B) for a kink located at point (A); a), b) influence of the kink length, c), d) influence of the kink angle, (*F* according to eq.(2.2)).

The geometric functions for the stress intensity factors at the kink (i.e. at location (A)) are represented in Fig. 5.6. Figures 5.6a and 5.6b show the mixed-mode stress intensity factors for the crack tip located at point (A) The mode-I stress intensity factor is also hardly affected by the kink. In contrast to point (B), the mode-II stress intensity factor is roughly proportional to the square root of the kink length. Figures 5.6c and 5.6d show the influence of the kink angle φ. The mode-II stress intensity factor K_{II} at point (A) is also proportional to the kink angle.

$$K_{II,(A)} \propto \sqrt{\ell / a}\,\varphi \tag{5.8}$$

The geometric functions for the stress intensity factors at the kink (i.e. at location (A)) are represented in Fig. 5.6.

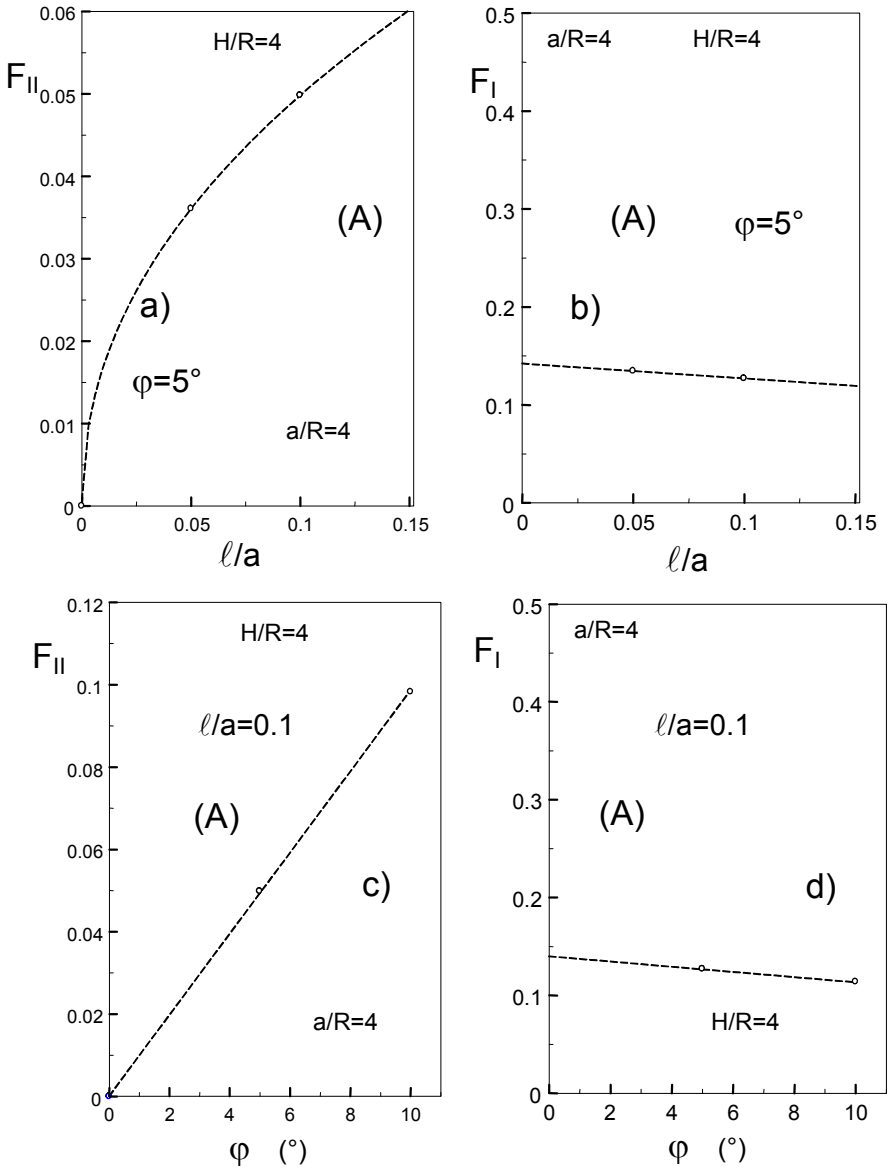

Fig. 5.6 Mixed-mode stress intensity factors at point (A) for a kink located at point (A); a), b) influence of the kink length, c), d) influence of the kink angle, (*F* according to eq.(2.2)).

6. Short-crack behaviour

6.1 Limit case $R/H \to 0$

The most important fracture mechanics properties of small cracks emanating from the hole of a DCDC specimen can be discussed on the basis of the limit case of a small hole compared to the other dimensions of the specimen, i.e. for $R/H \to 0$. The stresses in polar coordinates are [14]

$$\sigma_r = -\tfrac{1}{2} \mid p \mid \left[1 - \left(\frac{R}{x+R} \right)^2 + \left(1 + 3 \left(\frac{R}{x+R} \right)^4 - 4 \left(\frac{R}{x+R} \right)^2 \right) \cos(2\varphi) \right] \tag{6.1}$$

$$\sigma_\varphi = -\tfrac{1}{2} \mid p \mid \left[1 + \left(\frac{R}{x+R} \right)^2 - \left(1 + 3 \left(\frac{R}{x+R} \right)^4 \right) \cos(2\varphi) \right] \tag{6.2}$$

$$\tau_{r\varphi} = \tfrac{1}{2} \mid p \mid \left[1 - 3 \left(\frac{R}{x+R} \right)^4 + 2 \left(\frac{R}{x+R} \right)^2 \sin(2\varphi) \right] \tag{6.3}$$

with the polar angle defined in Fig. 6.1.

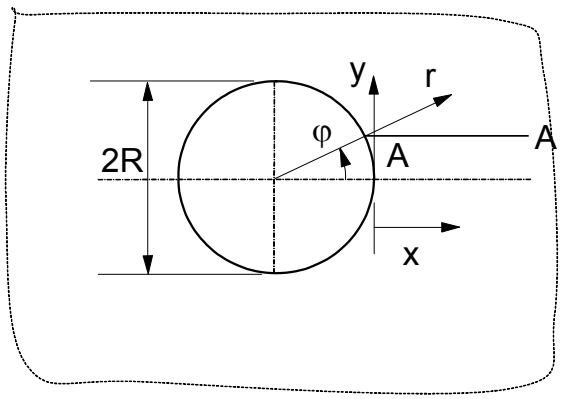

Fig. 6.1 Polar and Cartesian coordinates for a circular hole in an infinite plate.

The stress components in Cartesian coordinates result from the transformations

$$\sigma_x = \sigma_r \cos^2(\varphi) + \sigma_\varphi \sin^2(\varphi) - 2\tau_{r\varphi} \sin(\varphi)\cos(\varphi) \tag{6.4}$$

$$\sigma_y = \sigma_r \sin^2(\varphi) + \sigma_\varphi \cos^2(\varphi) + 2\tau_{r\varphi} \sin(\varphi)\cos(\varphi) \tag{6.5}$$

$$\tau_{xy} = (\sigma_r - \sigma_\varphi)\sin(\varphi)\cos(\varphi) + \tau_{r\varphi}(\cos^2(\varphi) - \sin^2(\varphi)) \tag{6.6}$$

The normal and shear stresses are evaluated along the line A-A in Fig. 6.1 at y/R=0.01. The results are represented in Fig. 6.2. Since the shear stresses are proportional to the y-offset for small y/R, the shear stresses are multiplied by the factor R/y. The influence of such a small offset can be neglected for the normal stresses σ_y.

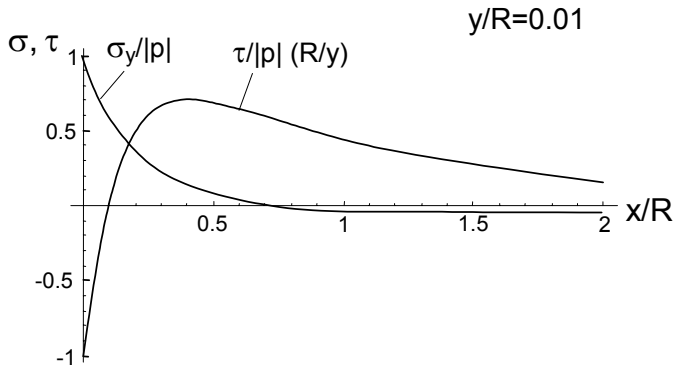

Fig. 6.2 Normal and shear stresses along the line A-A in Fig. 6.1 with a y-offset of y/R=0.01.

Along the line y=0, no shear stresses occur for reasons of symmetry. At a positive y, the shear stresses are positive, axcept for a small region x/R<0.1. The shear stresses at negative y exhibit the inverse sign. The gradient in the shear stresses results from eqs.(6.1-6.6)

$$\frac{d(\tau / |p|)}{d(y/R)} = -\frac{1-10(x/R)-5(x/R)^2}{(1+(x/R))^5} \tag{6.7}$$

as plotted in Fig. 6.3. A change of the sign of shear stresses is obtained for x/R=0.095.

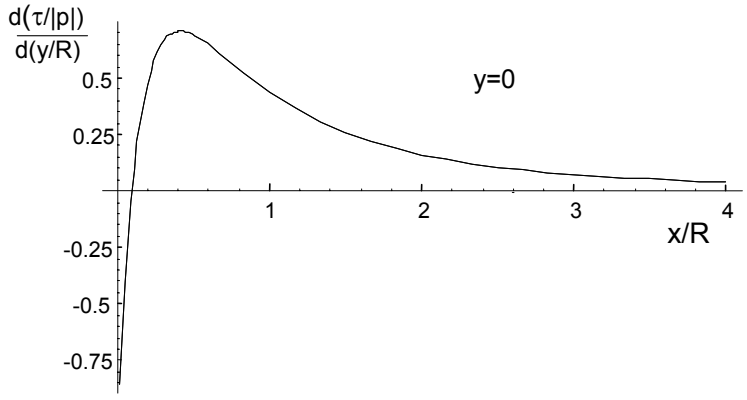

Fig. 6.3 Gradient of the shear stresses, dτ/dy, along the symmetry line y=0.

From the stresses of Fig. 6.2, the mixed-mode stress intensity factors K_{I} and K_{II} were computed for cracks emanating from the hole along the line A-A according to eqs.(3.1) and (3.2) with the weight function h_{I} from eq.(3.3). For the mode-II stress intensity factor, the asymptotic weight function

$$h_{II} \cong \sqrt{\frac{2}{\pi(a-x)}} \tag{6.8}$$

was used. The results are plotted in Fig. 6.4 in the form of the geometric functions defined by eq.(2.2) for the mode-I case and

$$F_{II} = \frac{K_{II}}{|\,p\,|\sqrt{\pi R}} \tag{6.9}$$

for mode II.

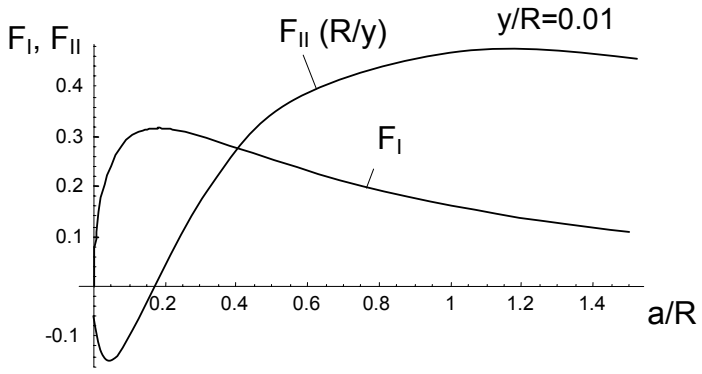

Fig. 6.4 Mixed-mode stress intensity factors for small cracks emanating from a hole in an infinite body having a small offset from the symmetry line.

6.2 Influence of finite specimen height

The finite specimen height affects the stresses as shown in Fig. 6.5. In this diagram, the normal stresses σ_y are plotted for the case of y=0 (the shear stresses disappear for reasons of symmetry). Finite element results are plotted as solid curves for the case of H/R=4. The dashed curves again represent the stresses for the hole in an infinite body. A comparison of the shear stresses (finite element results obtained for y/R=0.0666) is given in Fig. 6.6.

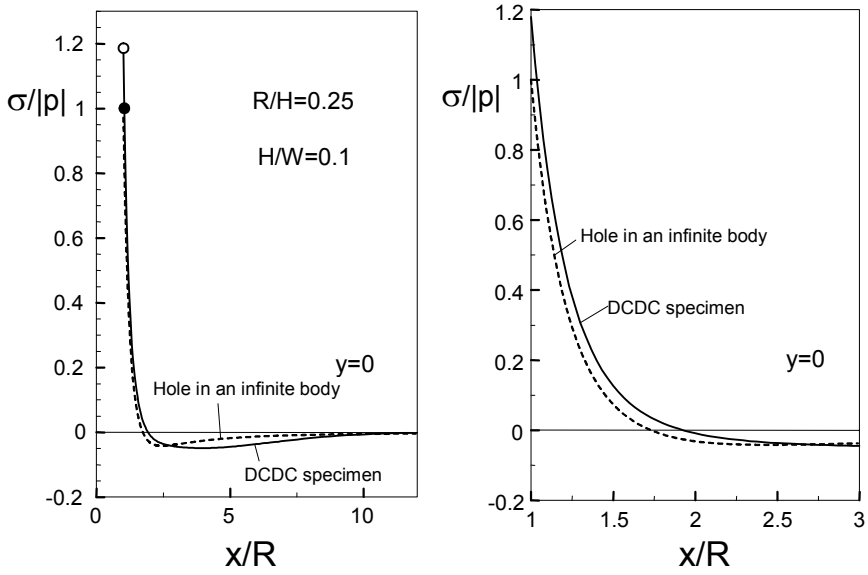

Fig. 6.5 Normal stresses along the line y=0 for a DCDC specimen and the infinite body solution.

Comparing the stresses obtained from the analytical solutions for the hole in an infinite body with the finite element results gives a very good agreement for the σ_x and τ_{xy} stress components near the symmetry line y=0. Only the σ_y stress shows significant deviations. In this case, the finite element solution should be preferred.

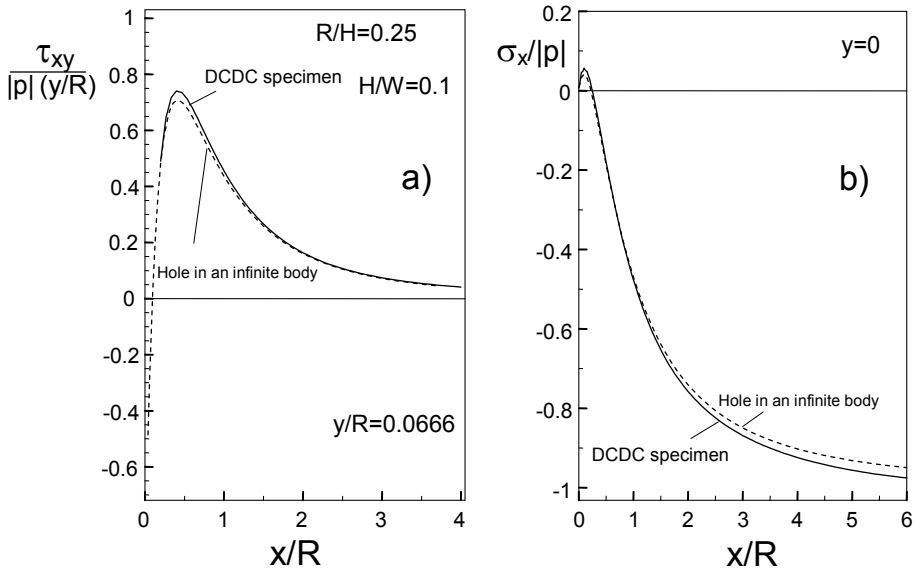

Fig. 6.6 a) Shear stresses along the line y=0.0666 R for a DCDC specimen (solid curve) compared with the solution for an infinite body, b) x-stress along y=0.

The good agreement of the shear stresses, for instance, allows the application of the analytically given stress solution for further computations. One possibility is the determination of mode-II stress intensity factors for cracks deviating slightly from the symmetry line. In this case, the stresses in the uncracked specimen are of interest.

For the stresses near the hole, the mode-I stress intensity factor was computed from the σ_y stresses obtained by the finite element analysis. Figure 6.7a shows the results obtained from eq.(3.1) and the weight function for small cracks, eq.(3.3), as the squares. The finite element results for large cracks are represented by the dashed line. An interpolation of these two solutions results in the continuous curve of Fig. 6.7b that covers short- and long-crack behaviour.

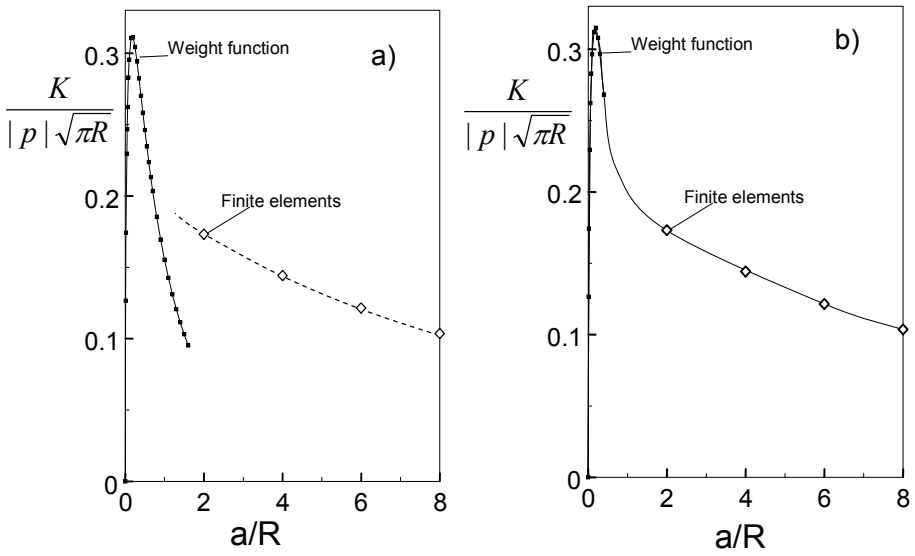

Fig. 6.7 Mode stress intensity factors for cracks emanating from a hole in a DCDC specimen of H/R=4. a) Solid curve: solution obtained with the weight function, eqs.(3.1) and (3.3), dashed curve: finite element results, b) interpolation of the two solutions.

7. Spontaneous crack propagation

The special shape of the stress intensity factor vs. crack length curve gives rise to an unstable extension of cracks introduced at the circumference of the hole during the drilling procedure. First, the $K(a)$ curve increases until a maximum of $K/|p|\sqrt{(\pi R)}\cong 0.31$ is reached at a crack length of $a/R\cong 0.2$. Then, the stress intensity factor decreases monotonically with increasing a. Figure 7.1 shows this behaviour for K^2 in order to allow for a discussion in terms of the energy release rate G, given by

$$G = \frac{K^2}{E'} \tag{7.1}$$

where E' is the plane strain modulus.

In Fig. 7.1a, a maximum initial crack of depth $a_i/R=0.08$ is assumed to exist at the bore hole. This crack starts spontaneously and extends at a critical compressive stress p_c, for which

$$|\, p_c \,| = \frac{K_{Ic}}{F\sqrt{\pi R}} \tag{7.2}$$

is fulfilled for the first time (K_{Ic}=fracture toughness). In this case, $F^2 \cong 0.08$. Under conditions of quasi-static crack extension, the crack would stop at the second intersection, as indicated by the solid arrow. During crack extension, F^2 and consequently also G are larger than the critical value (indicated by the dashed area above $F^2=0.08$). This area represents an excess of energy. Consequently, the spontaneously extending crack can stop only, if this energy is consumed. In the case of no energy being converted into heat, the crack will stop after a larger unstable crack extension phase up to an arrest crack length of $a_{arr}/R\cong 0.6$, indicated by the open arrow.

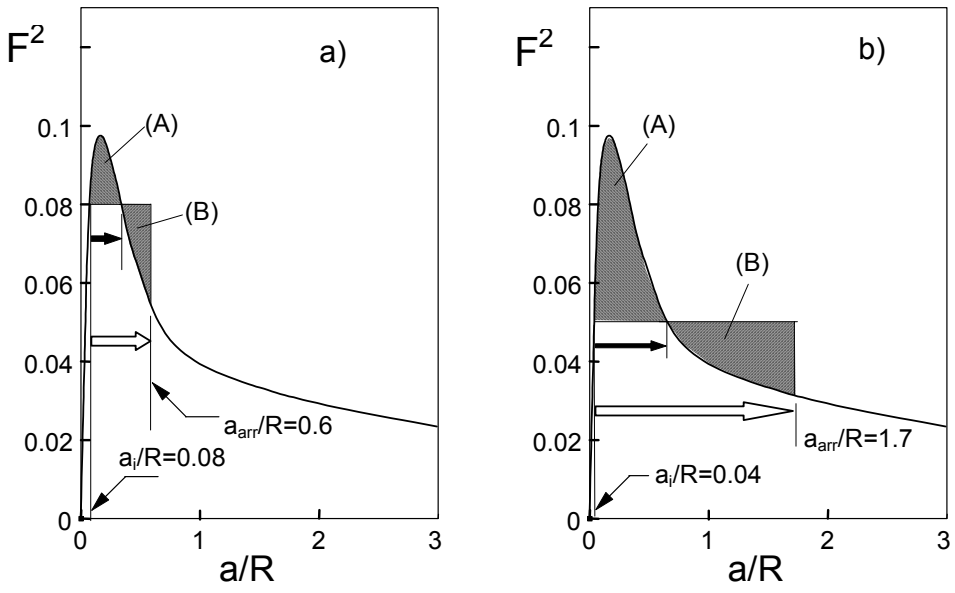

Fig. 7.1 Spontaneous crack extension for a crack of initial size $a_i/R=0.08$ (a) and $a_i/R=0.04$ (b). The shaded areas represent the energy excess resulting in an increased arrest crack length a_{arr}.

Figure 7.1b illustrates the crack extension of a smaller initial depth $a_i/R \cong 0.04$. In this case, a higher pressure is necessary to start crack extension, followed by a strongly extended spontaneous crack propagation phase. A final maximum crack length of $a_{arr}/R \cong 1.7$ will be reached.

Figure 7.2 shows the crack extension behaviour of large cracks. If the initial crack depth is larger than the crack length corresponding to the maximum value of the F^2 vs. a/R curve, $a_{max}/R=0.2$, a stable situation is obtained, as indicated by the circle. At this location, $K=K_{Ic}$ is reached (Fig. 7.2a). Extension of this crack is possible only under *increasing* pressure p. Crack extension is also possible under a *fixed load* for materials which show the effect of subcritical crack growth, i.e. crack growth at $K<K_{Ic}$.

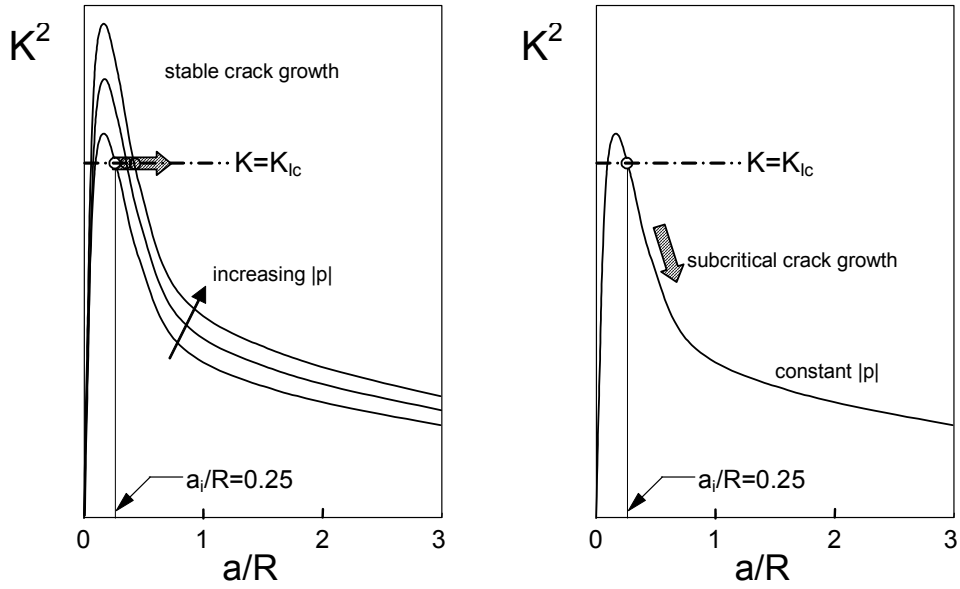

Fig. 7.2 Quasi-static crack extension of a large crack of initial size $a_i/R=0.25$; a) stable crack extension under monotonously increasing loading, b) crack extension under subcritical crack growth conditions.

8. 3-dimensional analysis

8.1 Straight crack

In [3], Celarie et al. present measurements of the free surface height profile near the tip of a crack growing in soda-lime glass. They used the DCDC specimen and measured uplifting and depression using an atomic force microscope (AFM). Celarie et al.[3] interpret the surface profiles near the crack tip as a consequence of plastic deformations. This section shall focus on the out-of-plane displacements near the crack tip that result from the elastic behaviour of the cracked DCDC specimen.

8.1.1 Stress intensity factor and T-stress

The numerical results are plotted in Figs. 8.1, 8.2, and 8.3. Figure 8.1a shows the σ_{yy} stresses at the free surface in a logarithmic representation. From this plot, it can be concluded that the near-tip stress field related to the stress intensity factor dominates up to $x/W \approx 0.001$, which is obtained from the deviations from the –1/2 slope of the plot. In Fig. 8.1b, the change of the stress intensity factor along the straight crack is shown. A very strong variation of the geometric function F is visible. It decreases to a value of roughly 50% of that in the inner zone. As expected, the 2-D result of He et al.[1] (dash-dotted line) is the average of the local values. Figure 8.1c shows the T-stress over the cross-section. The variation of this fracture mechanics parameter is smaller compared to the stress intensity factor.

As a further parameter representing the stress state at the crack tip, the strain ε_{zz} parallel to the crack tip line was computed.

Below, interest shall be limited to the z-displacement variations over a surface region very close to the crack tip. Figure 8.2a shows the strain in thickness direction, ε_{zz}, over the thickness B at several distances from the crack tip. From this representation, we can conclude that nearly over the whole thickness of the specimen the z-strains are identical. These strains independent of x cannot contribute to the variation of surface displacement with x, since

$$\int_{\substack{centre\\region}} \varepsilon_{zz}\, dz \neq f(x) \tag{8.1}$$

Only the near-surface strains show a dependency on x and, therefore, have to be responsible for the variation of u_z.

Figure 8.2b shows the details near z/B=-0.5 for different distances from the crack tip. The arrows indicate the locations (z_d) where first deviations from the common curve for ε_{zz} are visible. In Fig. 8.2c, these depths from the surface are plotted versus the distance from the crack tip.

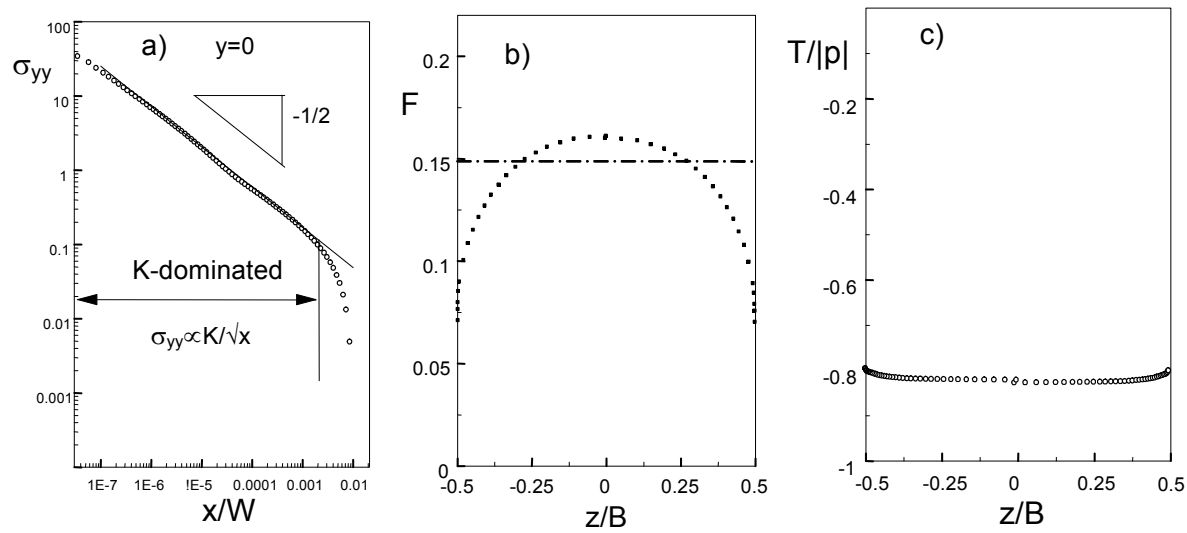

Fig. 8.1 a) Stresses σ_{yy} at the specimen surface along the line y=0, b) variation of the stress intensity factor along the straight crack, c) variation of T-stress.

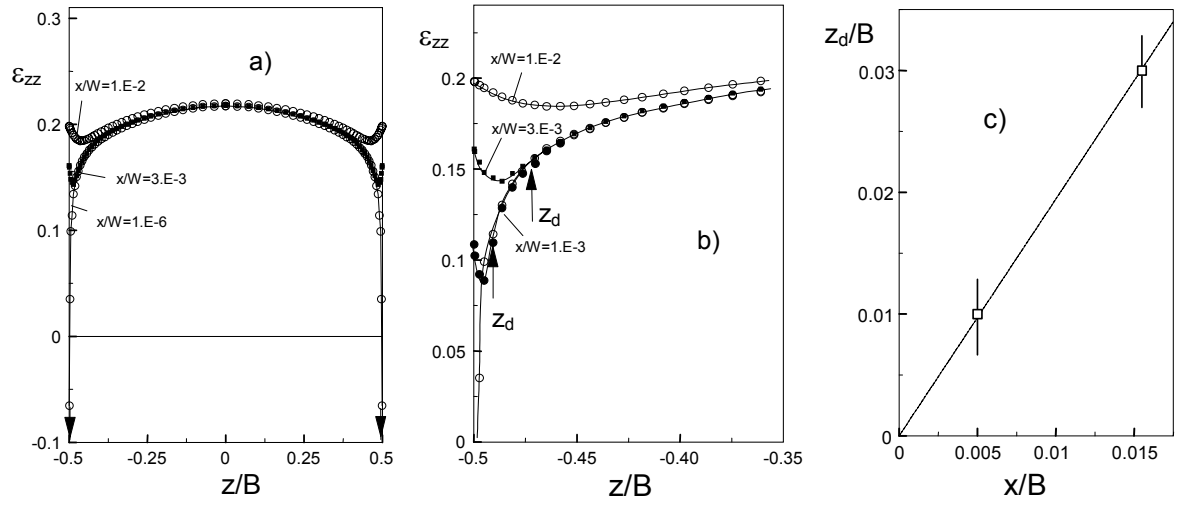

Fig. 8.2 a) z-strains over the cross-section at several distances from the crack tip, b) detail near z/B=-0.5 (arrows: first deviation from the common curve), c) depth of first deviation versus distance from the crack tip.

8.1.2 Surface displacements

In Figs. 8.3a and 8.3b, the out-of-plane surface displacements are shown along the line y=0 (i.e. in the crack plane). In the 3-D finite element model, several numbers of elements over the specimen thickness were chosen. The element size decreased continuously while approaching the free surfaces. The two outer elements were drastically reduced to 1/100 and 1/10 of the smallest element of the bulk material. From this short convergence study, it was concluded that the finest mesh with 40 thickness elements in total is sufficient to provide correct u_z displacements. For further numerical computations, the 40-element net was used.

For large distances from the crack tip, the displacements tend to the limit case of a specimen without a crack: u_z=-νB/2.

Figures 8.3c and 8.3d represent the u_z displacements at the free surface along lines x/W=-0.02, 0, and 0.02.

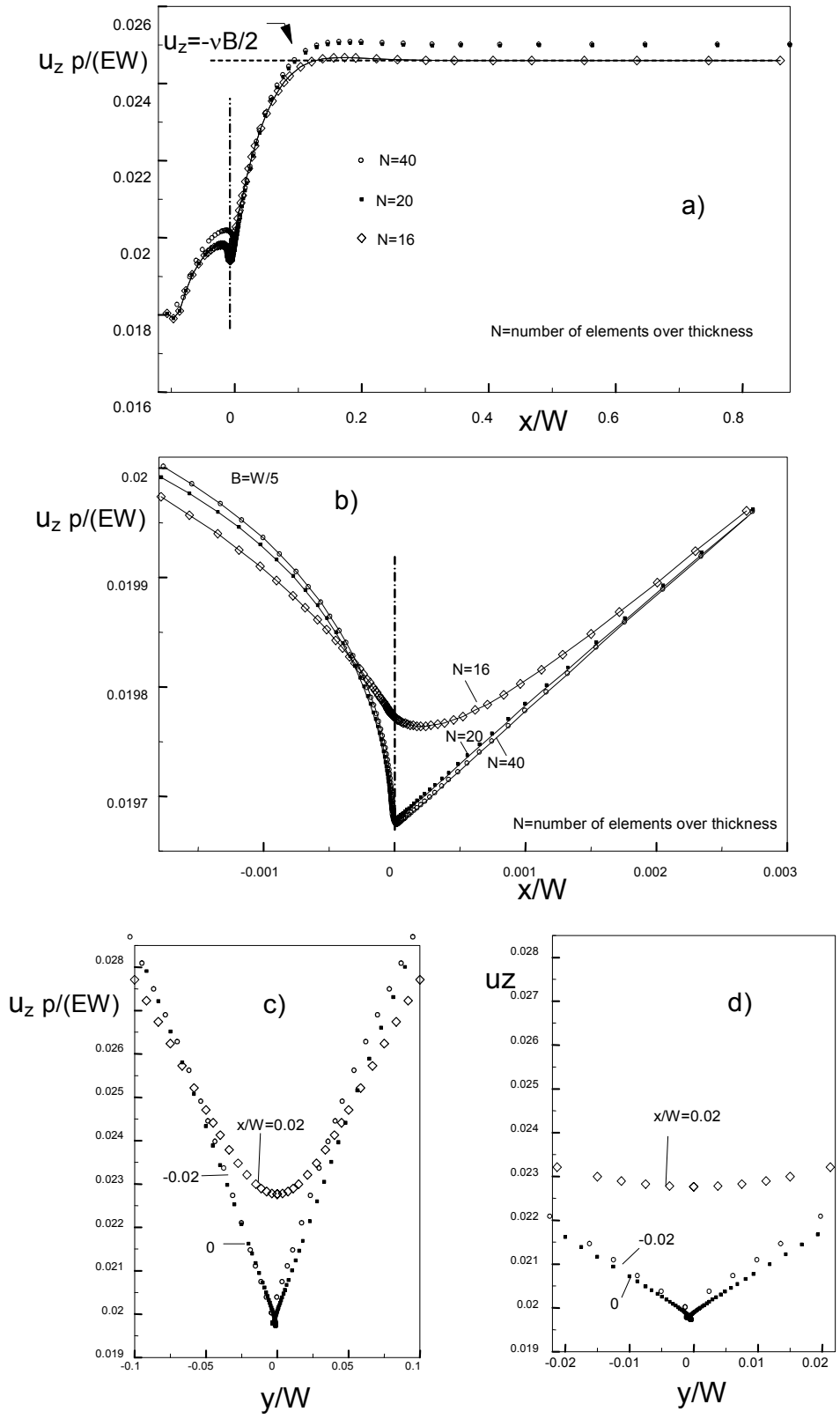

Fig. 8.3 a), b) Out-of-plane displacement u_z along y=0, c), d) out-of-plane displacement along x/W= –0.02, 0, and +0.02 (for N=40 elements over the thickness).

8.2 Influence of a curved crack front

In the experiments by Celarie et al.[3], a curved crack front was found (Fig. 8.4a). This is a consequence of the reduced stress intensity factors in the surface region (see Fig. 8.1b), resulting in a reduced crack growth. As a consequence, the near-tip stresses normal to the crack front, $\sigma_{\xi\xi}$, given by

$$\sigma_{\xi\xi} = \frac{K}{\sqrt{2\pi\xi}} \tag{8.2}$$

are no longer parallel to the outer surface, but generate a stress component normal to the free surface σ_{zz}, which, under plane stress conditions in the near-surface region ($\Rightarrow\sigma_{\xi\xi}=0$), is given as

$$\sigma_{zz} = \sigma_{\xi\xi}\cos^2\varphi = \frac{K}{\sqrt{2\pi\xi}}\cos^2\varphi \tag{8.3}$$

Since no tractions are present on the free surface that can balance the near-tip tensile stress σ_{zz}, the surface region next to the crack tip must become more dented. This effect is visible from the FE results.

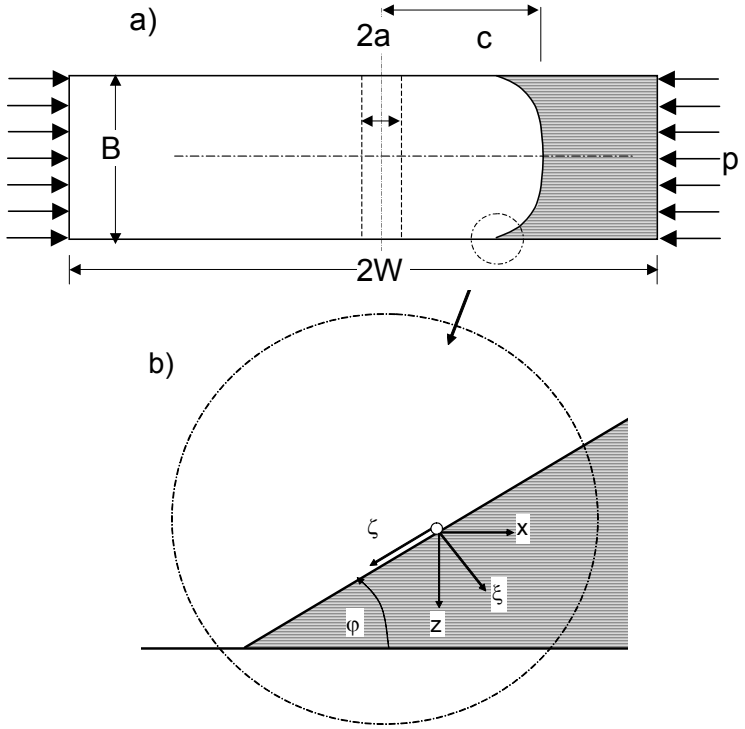

Fig. 8.4 a) DCDC specimen with a curved crack front, b) detail of a).

Figure 8.5a shows the crack approximated by straight segments. The outer crack part intersects the free surface under an angle of φ (φ=90° corresponds to the straight crack). The next deeper part was modelled as a straight line with an intermediate angle of (φ+90°)/2. The geometric function of the local stress intensity factor is plotted in Fig. 8.5b for φ=90° and 60°. The u_z displacements at the free surface are shown in Fig. 8.6. For the different angles 45°, 60°, and 90°, a similar displacement behaviour was found. The variation of u_z becomes stronger with a decreasing angle φ.

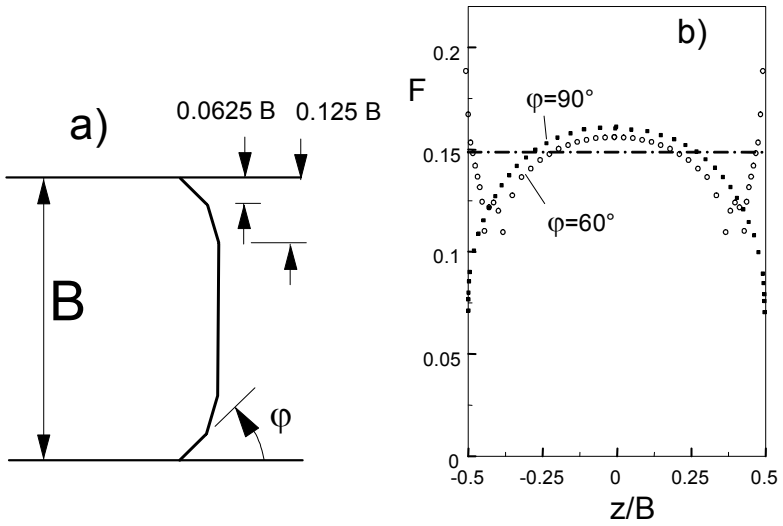

Fig. 8.5 a) Curved crack front approximated by straight segments, b) stress intensity factor along the crack tip line.

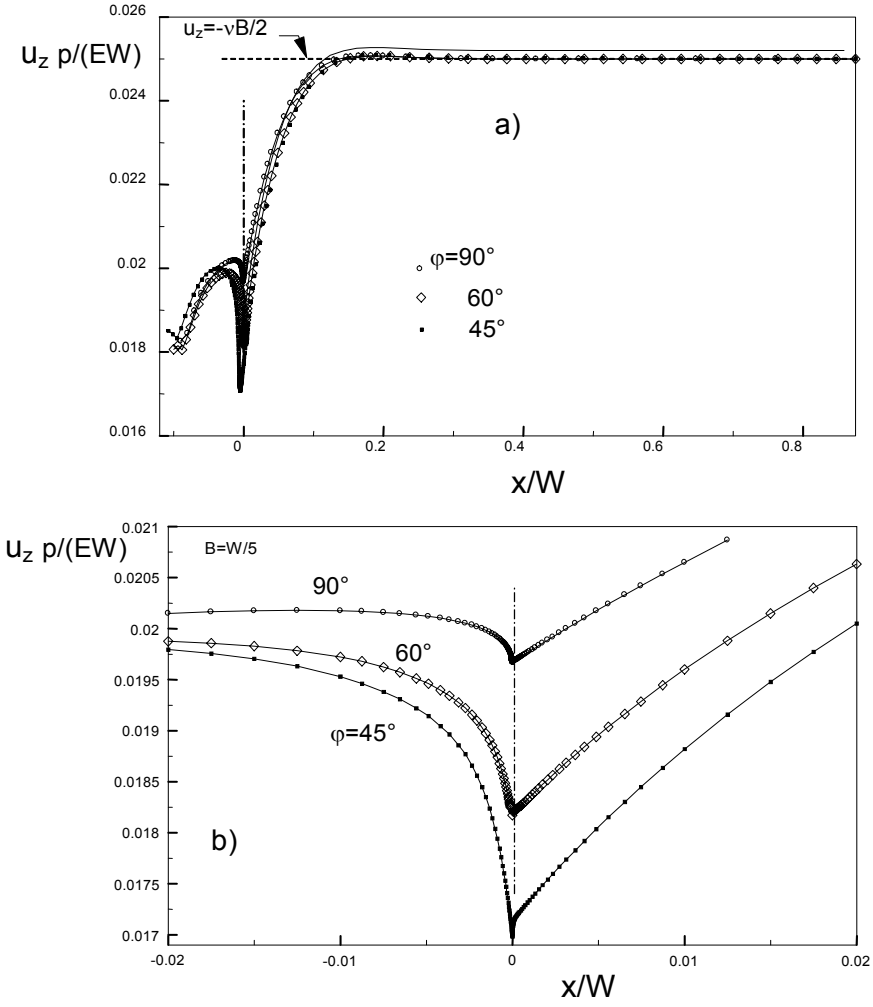

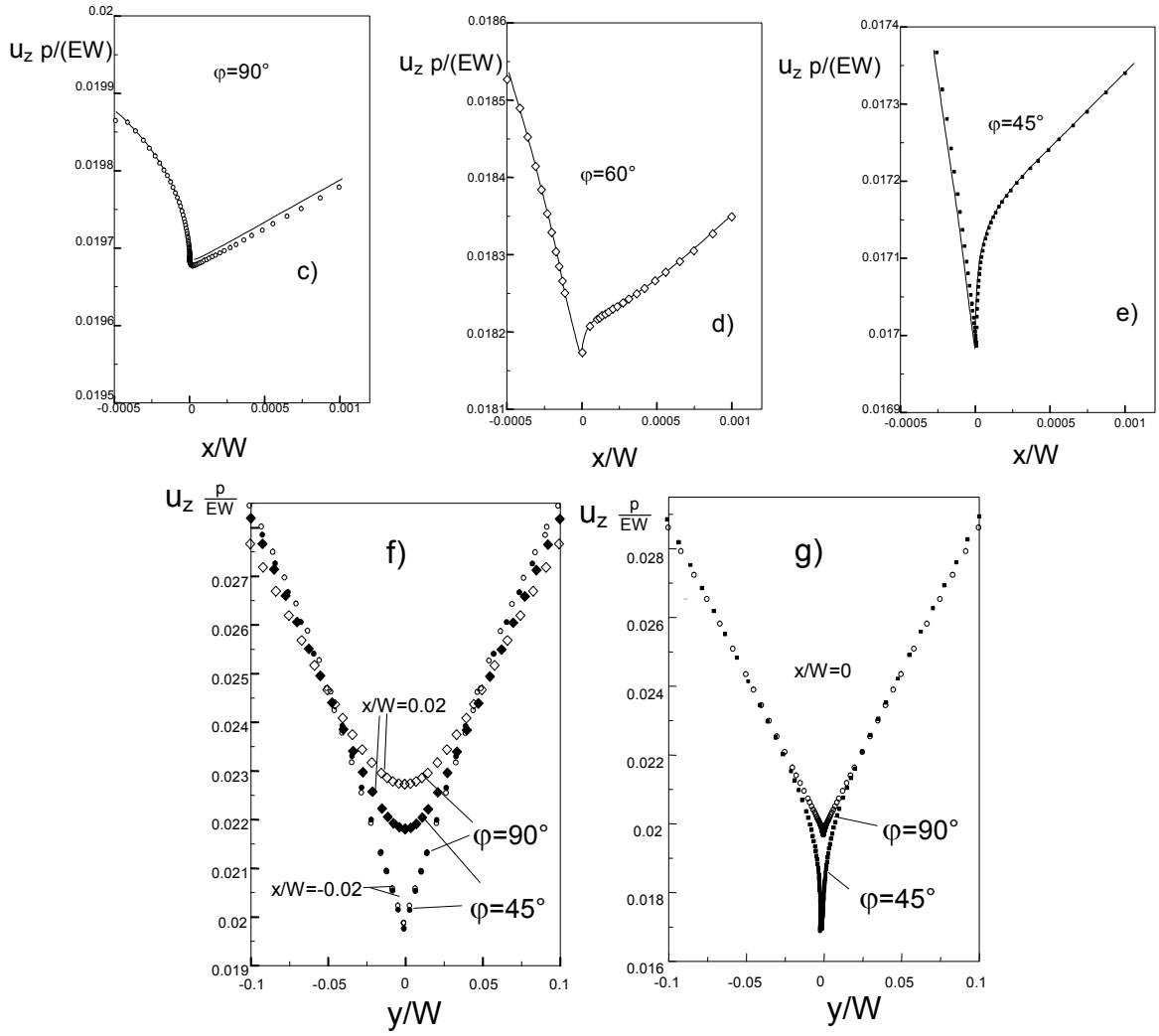

Fig. 8.6 a) u_z displacements obtained for φ=90°, 60°, and 45°, b) detail near x/W=0 (computations performed with 40 elements over the thickness), c), d), e) details of b), f), g) z-displacements along lines x=constant.

The purely elastic analysis described in this section reveals out-of-plane displacements which are in best agreement with the measurements of Celarie et al.[3]. From this point of view, there is no indication of a "plastic" material behaviour of glass.

9. A modification of the path stability relation for DCDC specimens

In this section, it is made use of a relation for the mode-II stress intensity factor derived by Goldstein and Sagalnik [15] and applied successfully by Melin [16,17]. Since the integral equation derived in [15] is only applicable to constant stresses σ_x and σ_y acting far away from the considered crack, a modification has to be made, taking into account the strongly varying stress state, for instance, near the hole of the DCDC specimen. Therefore, let us derive the appropriate equations similar to [18].

In a first-order approximation, the mode-II stress intensity factor caused by the mode-I contribution due to kinking can be written (see [15-18]) as

$$K_{II,1} = \tfrac{1}{2}\left(y'\big|_{x=a} - \frac{y(a)}{a} \right) K_I \tag{9.1}$$

where y' and $y(a)/a$ are assumed to be very small.

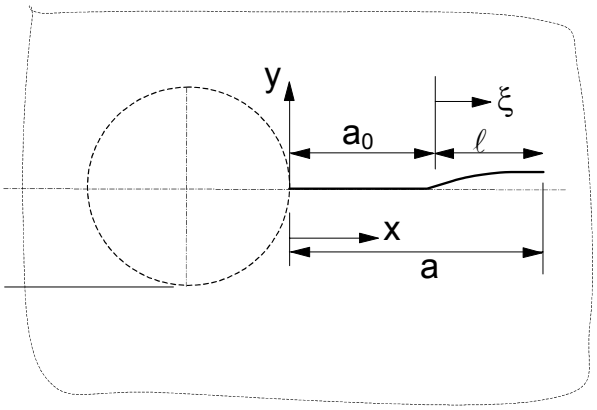

Fig. 9.1 Crack deviating from the symmetry line.

The mode-II contribution caused by a rotated crack plane, $K_{II,2}$, is given as

$$K_{II,2} = \int_0^a (\sigma_{y,0} - \sigma_{x,0})\, h_{II}\, y'(x)\, dx \tag{9.2}$$

where $\sigma_{y,0}$ and $\sigma_{x,0}$ are the y- and x- stresses along the symmetry line (i.e. at y=0) in the uncracked component.

As can be seen from Figs. 6.2 and 6.6a, a shear stress occurs for $y \neq 0$. If the crack deviates from the symmetry line, these shear stresses also contribute a mode-II stress intensity factor, $K_{II,3}$, as shown in Fig. 6.4 for instance. For this stress intensity factor, it holds

$$K_{II,3} = \int_0^a \frac{d\tau_{xy}}{dy}\, y(x)\, h_{II}\, dy \tag{9.3}$$

and the total mode-II stress intensity factor results as

$$K_{II} = \tfrac{1}{2}\left(y'\big|_{x=a} - \frac{y(a)}{a} \right) K_I + \int_0^a \left((\sigma_{y,0} - \sigma_{x,0}) y'(x) + \left.\frac{d\tau_{xy}}{dy}\right|_{y=0} y(x) \right) h_{II}\, dx \tag{9.4}$$

From the crack growth condition K_{II}=0, we obtain the integral equation

$$y'\big|_{x=a} - \frac{y(a)}{a} + \frac{2}{K_I}\int_0^a \left((\sigma_{y,0} - \sigma_{x,0})y'(x) + \left.\frac{d\tau_{xy}}{dy}\right|_{y=0} y(x) \right) h_{II}\, dx = 0 \qquad (9.5)$$

For a numerical analysis of path stability of DCDC cracks, the term $y(a)/a$ in (9.5) can be neglected.

References

[1] He, M.Y., Turner, M.R., Evans, A.G. (1995), Analysis of the double cleavage drilled compression specimen for interface fracture energy measurements over a range of mode mixities, Acta metall. mater. **43**, 3453-3458.

[2] Ritter, J.E., Huseinovic, A., Chakravarthy, S., Lardner, T.J. (2000), Subcritical crack growth in soda-lime glass under mixed-mode loading, J. Amer. Ceram. Soc. **83**, 2109-2111.

[3] F. Célarié, S Prades, D. Bonamy, L. Ferrero, E. Bouchaud, C. Guillot, and C. Marlière, Glass breaks like metals, but at the nanometer scale, *Phys. Rev. Let.*, **90** [7] 075504 (2003).

[4] Maliere, C., Despetis, F., Phalippou, J., Crack path instabilities in DCDC experiments in the low speed regime, J. of Non-Crystalline Solids 316(2003), 21-27.

[5] Lardner, T.J., Chakravarthy, S., Quinn, J.D., Ritter, J.E. (2001), Further analysis of the DCDC specimen with an offset hole, Int. J. Fract. **109**, 227-237.

[6] T. Fett, G. Rizzi, D. Munz, T-stress solution for DCDC specimens, Engng. Fract. Mech. **72**(2005), 145-149.

[7] Leevers, P.S., Radon, J.C. (1982), Inherent stress biaxiality in various fracture specimen geometries, Int. J. Fract. **19**, 311-325.

[8] Cotterell, B. and Rice, J.R. (1980), Slightly curved or kinked cracks, *International Journal of Fracture* **16**, 155-169.

[9] Melin, S. (1991), On the directional stability of wedging, Int. J. Fract. **50**, 293-300.

[10] Melin, S. (2002), The influence of the T-stress on the directional stability of cracks, Int. J. Fract. **114**, 259-265.

[11] T. Fett, D. Munz, Stress intensity factors and weight functions, Computational Mechanics Publications, 1997, Southampton.

[12] Shih, C.F., Asaro, R.J. (1988), Elastic-plastic analysis of cracks on biomaterial interfaces: Part I – Small scale yielding, J. Appl. Mech., 299-316.

[13] He, M.Y., Bartlett, A., Evans, A.G., Hutchinson, J.W., Kinking of a crack out of an interface: role of in-plane stress, J. Am. Ceram. Soc. **74**(1991), 767-771.

[14] Timoshenko, S.P., Goodier, J.N. (1970), Theory of Elasticity, McGraw-Hill, Kogakusha.

[15] R.V. Goldstein and R.L. Salganik, Brittle fracture of solids with arbitrary cracks, Int. J. Fracture, 10 (1974) 507-523

[16] S. Melin, On the directional stability of wedging, Int. J. Fracture 50 (1991) 293-300.

[17] S. Melin, Directional stability of an originally straight crack, Int. J. Fracture 53 (1992) 121-128.

[18] V.-B. Pham, H.-A. Bahr, U. Bahr, T. Fett, H. Balke, Crack paths and directional stability of cracks in homogeneously stressed infinite and semi-infinite plates, submitted to Int. J. Fract.